Identifying and Tuning the In Situ Oxygen-Rich Surface of Molybdenum Nitride Electrocatalysts for Oxygen Reduction

Michaela Burke Stevens[1,2]†, Melissa E. Kreider[1,2]†, Anjli M. Patel[1,2], Zhenbin Wang[3], Yunzhi Liu[4], Brenna M. Gibbons[2,4], Michael J. Statt[1,2], Anton V. Ievlev[5], Robert Sinclair[4], Apurva Mehta[6,7], Ryan C. Davis[6,7], Jens K. Nørskov[3], Alessandro Gallo[2,6], Laurie A. King[8*], Thomas F. Jaramillo[1,2*]

† These authors contributed equally

* Corresponding authors (jaramillo@stanford.edu and L.King@mmu.ac.uk)

1) Department of Chemical Engineering, Stanford University 443 Via Ortega, Stanford, CA 94305, USA

2) SUNCAT Center for Interface Science and Catalysis, SLAC National Accelerator Laboratory, Menlo Park, CA 94025, USA

3) Department of Physics, Technical University of Denmark, 2800 Kongens Lyngby, Denmark

4) Department of Materials Science and Engineering, Stanford University, 496 Lomita Mall, Stanford, CA 94305

5) Center for Nanophase Materials Sciences, Oakridge National Laboratory, Oak Ridge, TN 37831, USA

6) SLAC National Accelerator Laboratory, 2575 Sand Hill Road, Menlo Park, CA, USA

7) Stanford Synchrotron Radiation Lightsource, SLAC National Accelerator Laboratory, Menlo Park, CA 94025, USA

8) Faculty of Science and Engineering, Manchester Metropolitan University, Chester Street, Manchester, M1 5GD, UK

Abstract

Rigorous in situ studies of electrocatalysts are required to enable the design of higher performing catalysts. Non-platinum group metals for oxygen reduction (ORR) catalysis containing light elements such as oxygen, nitrogen, and carbon are known to be susceptible to both ex situ and in situ oxidation leading to challenges associated with ex situ characterization methods. We have previously shown that bulk O content plays an important role in the activity and selectivity of Mo-N catalysts, but further understanding the role of composition and morphological changes at the surface is needed. Here, we report the measurement of in situ surface changes to a molybdenum nitride (MoN) thin film under ORR conditions using grazing incidence x-ray absorption and

reflectivity. We show that the halfwave potential of MoN can be improved by ~ 90 mV by potential conditioning up to 0.8 V vs RHE. Utilizing electrochemical analysis, dissolution monitoring, and surface sensitive x-ray techniques, we show that under moderate polarization (0.3 – 0.7 V vs RHE) there is local ligand distortion, O incorporation, and amorphization of the MoN surface, without changes in roughness. Furthermore, with a controlled potential hold procedure, we show that the surface changes concurrent with potential conditioning are stable under ORR relevant potentials. Conversely, at higher potentials (≥ 0.8 V vs RHE) the film incorporates O, dissolves, and roughens, suggesting that in this higher potential regime the performance enhancements are due to increased access to active sites. Density functional theory calculations and Pourbaix analysis provide insight into film stability and oxygen incorporation as a function of potential. These findings coupled with in situ electrochemical-surface sensitive x-ray techniques demonstrate an approach to studying non-traditional surfaces in which we can leverage our understanding of surface dynamics to improve performance with the rational, in situ tuning of active sites.

Keywords: oxygen reduction, electrocatalysis, in situ, molybdenum nitride, surface oxidation, grazing incidence x-ray absorption spectroscopy

TOC:

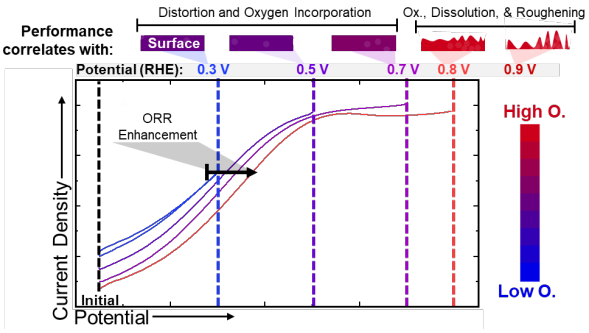

1.0 Introduction

Fuel cells, reactors that convert chemical bonds into electrical energy, have become increasingly important for a variety of applications in energy, including transportation and stationary, backup, and portable power due to their wide range in power levels (mW – MW) and fuel sources (hydrogen, methanol, etc.).[1] Hydrogen fuel cells are one promising technology in the effort to alleviate global climate change by reducing worldwide carbon emissions.[2–7] The efficiency of hydrogen fuel cells is limited, in part, by the rate, stability, and selectivity of the reduction of

oxygen to water (oxygen reduction reaction, ORR) at the cathode. Currently, platinum-based materials are the most extensively studied catalysts, due to their high activity, selectivity, and stability in both acidic and alkaline conditions.[8] Largely due to well-defined operando and in situ studies, Pt surface processes during catalysis, including the surface coverage,[9] predominant adsorbates,[10] reaction mechanism,[11] and degradation mechanism,[12] are well understood. This knowledge has been used successfully to reduce total Pt-loading in industrial systems by designing unique morphologies and alloys (e.g. Pt-Co).[13] To continue enhancing the practical utility of fuel cell technologies, however, further reduction or elimination of precious metal loading in PEMFCs is necessary.[14,15]

Metal-nitrogen-carbon (M-N-C) and transition metal nitride (TMN) catalysts have shown promise as non-platinum group metal alternatives for ORR catalysis.[16,17] However, extensive operando and in situ studies on both M-N-C and TMN materials have shown them to be highly susceptible to ex situ oxidation in air, as well as in situ electrochemical corrosion.[18–26] This suggests that in situ, the surface of many M-N-C and TMN catalysts is more oxidized (or contains more oxygen, O) than is intended based on the as-synthesized "pre-catalyst".[27,28] Typical ex situ characterization methods (e.g. x-ray diffraction, XRD), however, are not particularly well equipped to characterize this oxidized surface layer. Furthermore, the dynamic nature of catalyst surfaces, coupled with high surface area morphologies and complex active site compositions, makes it difficult to use ex situ properties to construct direct structure-activity relationships. There have been several studies showing oxynitrides to be interesting materials for ORR.[17,29,30] With a better understanding of the role that O plays in catalysis and in distorting the catalyst structure, new design strategies can be utilized to improve promising catalysts. Molybdenum nitride (Mo-N) based materials are one such promising catalyst class that has impressive material stability in acid, is relatively abundant, and has tunable H_2O_2 selectivity, but could benefit from substantial activity improvements, with a several hundred millivolt lower onset potential than Pt/C.[19,30–34]

Characterizing the active-surface dynamics of high surface area nanoparticulate catalysts (larger than 2 nm) is particularly challenging due to the complexity of differentiating between the surface and bulk of a nanoparticle in liquid electrolyte. In situ transmission electron microscopy is one promising technique for probing nanoparticulate catalyst systems, particularly for the analysis of structure and morphology. However, while this type of analysis has been particularly fruitful for

studying battery materials,[35] more development is necessary to overcome the challenges associated with obtaining surface sensitive compositional or structural information for electrocatalysts. There have been studies focusing on experimental techniques (e.g. ambient pressure x-ray photoelectron spectroscopy (XPS)) to measure the surface composition, structure, and adsorbate intermediates, including the light elements (e.g. O). However, these experiments are difficult to perform with liquid electrolyte, only probing the top surface of the catalyst, and are thus better suited for nanoparticle or high surface area configurations.[10,36] Grazing incidence (GI) characterization techniques, however, are particularly well-suited to distinguishing the surface from the bulk, allowing for improved analysis of in situ, surface-specific changes. Some GI techniques are also sensitive to compositional changes. For example, GI x-ray absorption spectroscopy (GI-XAS) has been used to study the temperature programmed reduction of GaN-supported Pt nanoparticles[37] and the in situ oxide layer thickness on thin film FeCr alloys during annealing.[38] Applying these techniques to electrocatalysis poses unique challenges due to the dynamic nature of surface changes and the presence of electrolyte and consequently, this has been less well-explored. Recently, an operando GI-XAS and XRD study on thin film Cu hydrogen evolution catalysts demonstrated the growth and reduction of an amorphous surface Cu oxide with applied potential.[39] This type of in situ surface compositional characterization for compound materials such as TMNs offers a promising route to developing in situ conditioning procedures to tune the material surface and optimize the catalytic performance and longevity.

In this work, we investigate the in situ surface-specific compositional and morphological changes on a thin film Mo-N oxygen reduction catalyst as a function of applied potential in acid. With ex situ XPS and time-of-flight ion mass spectrometry (ToF-SIMS), we demonstrate that, while O readily incorporates on the MoN surface as a function of time in air, there is no evidence for the incorporation of O into the bulk through air exposure or from ORR catalysis. Utilizing GI-XAS and x-ray reflectivity (XRR) to probe the surface in situ at ORR-relevant potentials in acid, we demonstrate local ligand distortion, amorphization, and oxidation of the surface as a function of increasing potential. Furthermore, we report that these changes coincide with enhanced ORR performance (90 mV decrease in overpotential at -2 mA cm_{geo}^{-2}). Combining these in situ measurements with studies of potential dependent electrochemical capacitance and Mo dissolution, we propose an in situ model of the MoN film as a function of applied potential that deconvolutes the surface from the bulk, differentiates ex situ vs in situ compositional changes, and

identifies changes in surface morphology. In this model, we hypothesize that potential cycling up to and including 0.7 V vs RHE enhances catalytic activity due to compositional and/or structural surface changes related to O incorporation. At potentials ≥ 0.8 V vs RHE, however, the catalyst is unstable, and we detect significant O incorporation, dissolution, and roughening, which also leads to activity enhancement at the expense of stability. Furthermore, our Mo-N-O-H Pourbaix diagram constructed from density functional theory (DFT) computations suggests that MoN becomes less thermodynamically stable with increasing potential, corresponding to a stronger driving force to convert to the more stable MoO_3 or MoO_2 species. This study highlights the importance of understanding the catalyst surface in situ to inform catalyst design and further demonstrates the possibilities of using electrochemical conditioning to develop unique and highly active catalyst materials.

2.0 Experimental

2.1 Materials. Used as received, without further purification unless otherwise stated: silicon wafers (WRS, 100 mm, P/Bor <100>, 10-20 Ohm-cm), glassy carbon electrodes (Pine Research Instrument, 0.196 cm^2 geometrical area), graphite counter electrode, Ag/AgCl reference electrode (Fisherbrand, Accumet), Mo sputtering target (Kurt J Lesker, 99.99% purity, 2" diameter), Ti sputtering target (Kurt J Lesker, 99.99% purity, 2" diameter), and perchloric acid (Honeywell Fluka, 70%).

2.2 Synthesis. A Lesker sputter tool was used to prepare molybdenum nitride thin films by DC reactive sputtering. Films were deposited on polished glassy carbon electrodes and Si wafers, using an HF etch to remove the native SiO_2 layer. A 10 nm Ti sticking layer was deposited first (2 minutes, 200 W power, 100% Ar atmosphere, 3 mTorr pressure). Without removing the sample from vacuum, the Mo target was sputtered first in 100% Ar for 1 minute and then in 100% N_2 atmosphere for 9 minutes to deposit ~30 nm of Mo-N. The chamber pressure was maintained at 6 mTorr, with a substrate temperature of 180 ± 10 ˚C with a substrate bias of (-) 110 V, and 200 W target power.[19]

2.3 Physical Characterization. XPS was performed using a Phi Versaprobe 3 with monochromatized Al Kα (1486 eV) radiation. The spectra were calibrated to the adventitious C 1s peak at 284.8 eV. Using CasaXPS software, peak fitting was performed with Shirley backgrounds

and Gaussian-Lorentzian line shapes. Details of the fits are included in the SI (**Table S1**, **Figure S1**).

ToF-SIMS measurements were conducted using the ToF.SIMS.5 NSC instrument (ION.TOF Gmb) at the Center for Nanophase Materials Sciences (CNMS) at Oak Ridge National Laboratory. The primary ion beam was a Bi_3^+ liquid metal gun (30 keV energy, 30 nA current, and 5 mm spot size). The secondary ions were analyzed using a time-of-flight mass analyzer in positive ion detection mode with mass resolution $m/\Delta m$ = 3,000 – 10,000. The depth profile sputter source was a Cs^+ ion beam (1 keV energy, 70 nA current, and 15 μm spot size). Measurements were performed in non-interlaced mode, with each scan by the Bi_3^+ primary beam followed by 5 s of sputtering with the Cs^+. $CsMo^+$, Cs_2O^+, and CsN^+ clusters were used to track concentrations of Mo^+, O^-, and N^-, respectively. SurfaceLab 7.0 (ION.TOF Gmb) software was used for data analysis.

XRR and grazing incidence XRD (GI-XRD) were performed at the Stanford Synchrotron Radiation Lightsource (SSRL) at SLAC National Laboratory on beamline 2-1. The 17 keV radiation was selected using a Si(111) monochromator. The Pilatus 100K detector was mounted ~700 mm from the sample. Two Soller slits were placed between the sample and the detector. XRD was collected at incident angles of 0.1 – 0.5˚, probing from the top 3 nm to the bulk of the sample. XRR models for ex situ samples were created using GenX and can be found in **Figure S2**. The Mo K-edge GI-XAS experiments were conducted at beamline 11-2 at SSRL. A monolithic 100-element Canberra germanium detector mounted at 90˚ angle to the incident beam was used to collect the energy resolved fluorescence signal with the ROI set on the Mo K-alpha feature. The photon energy was resolved and integrated with XIA DXP-XMAP digital photon processors. Scattered x-ray intensity was measured using a Pilatus 100K detector. Harmonics were eliminated using a Rh coated Si collimating mirror with a cutoff set at 21.5 keV. The incident energy was selected using a liquid N_2-cooled double crystal monochromator with Si(220) phi = 90˚ crystal cut. The incident beam was focused with a toroidal mirror to ca 300 um and apertured further with in hutch slits to ca 50 um. The energy was calibrated using a Mo metal foil and the first feature in the first derivative was assigned as 20 keV. Post-acquisition, the samples were re-aligned using a monochromator glitch that is stable and repeatable in energy. The surface and bulk of the film were probed using GI angles of 0.1 and 5˚, respectively. XAS spectra were normalized using the background subtraction and intensity normalization functions in the Athena software package[40]:

R_{bkg} = 1, k-weight = 2, pre-edge range -150 – -50, normalization range 150 – 550. Fourier transforms were made with a k-range = 3 – 11.1 Details of the extended x-ray absorption fine structure (EXAFS) fitting performed with the Artemis software are provided in the SI (**Table S2, Figure S3**).

ICP-OES was conducted with a Thermo Scientific ICAP 6300 Duo View Spectrometer using a solid-state CID detector. Samples were prepared via overnight dissolution in aqua regia (1:3 nitric acid : hydrochloric acid).

To prepare a cross-sectional transmission electron microscopy (TEM) specimen in the specific region tested during the in situ x-ray measurement, a FEI Helios NanoLab 600i DualBeam Focused Ion Beam/Scanning Electron Microscope (FIB/SEM) was used. First, a carbon protection layer was deposited using an electron beam, followed by the deposition of a Pt protection layer with a Ga^+ ion beam. The lamellae were then lifted out and milled using the Ga^+ ion beam with 30 keV energy to obtain an electron transparent region. The film was finally cleaned using an ion beam with energy 5 keV. The pre-test sample was prepared conventionally, by gluing the sample with epoxy to form a sandwich structure, cutting it, and mechanically polishing to 15 μm in thickness. To create an electron transparent region, the specimen was milled by an Ar^+ ion beam (5 keV, 5˚ incident angle) in a Gatan PIPS II ion milling machine. A FEI Titan Environment TEM was used to take high resolution (HR)-TEM images and selected area diffraction patterns (SADP), operating at 300 kV with an image corrector. The lattice and diffraction pattern of the Si substrate were used for calibration. The Oxford Xmax SDD Detector was used for scanning transmission electron microscopy energy-dispersive x-ray spectroscopy (STEM-EDS) analysis.

2.4 Electrochemical Testing. Electrochemical measurements were conducted in 0.1 M $HClO_4$ electrolyte purged with O_2 or N_2. The Ag/AgCl reference electrode was calibrated using a standard hydrogen electrode. The iR losses were compensated during the measurement at 85%, using the series resistance of the cell measured at 100 kHz. Electrochemical activity was measured using cyclic voltammetry using a Biologic VSP-300 Potentiostat. All voltammograms were corrected for background current by subtracting the N_2 baseline. Stability was evaluated using chronoamperometry. Unless otherwise specified, electrocatalysis measurements outside of the grazing incidence cell (GI-cell) were performed using a rotating disk electrode (Pine Research Instrument) in a 3-electrode glass cell with the catalyst deposited on a glassy carbon disk and a

graphite counter electrode. In situ measurements were performed in the GI-cell with the catalyst deposited on a doped-Si substrate and a Pt wire counter electrode. Although Pt electrodes are typically not used as anodes for ORR measurements (to mitigate sample contamination), in this configuration the distance between the Pt and sample surface and lack of stirring limited the risk of contamination. A cyclic voltammogram on the film after the XAS measurements exhibited no Pt features, supporting the hypothesis that Pt contamination did not occur. For the in situ cell, electrical connection is made to the thin film through a wire attached to the doped Si substrate and the wire is threaded through an isolated dry channel below the substrate. The electrolyte at the sample surface is connected via a series of channels to an O_2-bubbled electrolyte reservoir containing a Pt counter electrode and a Ag/AgCl reference electrode.

2.5 Computational Details. Density functional theory (DFT) calculations were performed using Vienna *ab initio* simulation package (VASP) within the projected-augmented wave method.[41,42] For the Pourbaix diagram calculation, the strongly constrained and appropriately normed (SCAN) functional was used for structure relaxations of all solid phases in the Pourbaix diagram with structures obtained from the Materials Project.[43,44] The plane wave energy cutoff was 520 eV. For the formation energy computations of O substitutional defects in cubic and hexagonal MoN, we employed the revised Perdew-Burke-Ernzerhof (RPBE) functional with a plane wave energy cutoff of 500 eV.[45] The electronic total energy and atomic force on the atoms in all structure relaxations were converged to 10^{-5} eV and 0.02 eV/Å, respectively. The Brillouin zone was sampled with a *k*-point density at least 1000/(number of atoms in the cell).[44] By following the Materials Project methods in addressing transition metal oxides,[46,47] we developed a Hubbard U value of 2.05 eV for Mo oxides by fitting to the experimental binary formation enthalpies in the Pourbaix diagram calculation. The SCAN Pourbaix diagram was constructed using the scheme developed by Persson et al. [48]

XANES Simulations

XANES at the Mo K-edge were simulated using FEFF9[49] for hexagonal MoN, cubic Mo_2N, and MoO_3 using the corresponding crystallographic structures (MoO_3: ICSD 80577; Mo_2N cubic: ICSD 251626; MoN hexagonal: ICSD 251629, from the NIST Inorganic Crystal Structure Database (ICSD)[50]). The simulations were performed using RPA-screened core hole and Hedin-Lundqvist self-energy. Convergence was checked for the self-consistent field potential calculation

and the full multiple scattering calculation and final values of 5 Å and 6 Å were utilized for SCF and FMS, respectively.

3.0 Results and Discussion

Mo-N catalysts have shown promising performance for the ORR in the nanoparticulate morphology with carbon binders.[31,34,51] In these systems, catalyst activity has been enhanced by increasing the nitrogen content (MoN > Mo_2N) and by doping with first-row transition metals (e.g. Co, Fe).[31,33,30] We have previously shown that Mo-N thin films can exhibit unexpectedly high O content in the bulk and that the ORR activity can be tuned by changing the bulk O:N:Mo ratio, with the most active compositions containing high N and low O content.[19] We have also demonstrated substantial *surface* oxidation as a function of time in air. This ex situ surface oxidation, in many compound metal systems (e.g. nitrides, sulfides, phosphides) highlights the uncertainty of the composition and structure of the active surface during ORR. Therefore, while bulk property-activity trends are important in guiding us to study active material classes, the characterization of in situ surface dynamics is necessary within a material class to develop methodologies that optimize activity, selectivity, and stability. To probe the scope of surface dynamics both ex situ and in situ, herein we have synthesized an ORR active MoN thin film (~30 nm) with low bulk oxygen content (< 5 %) that is comprised of small (~ 5 nm) crystallites with a mixture of rocksalt cubic and hexagonal structures (GI-XRD in **Figure S4**). Using a suite of ex situ and in situ characterization techniques, we construct a model of the MoN surface and bulk composition and morphology at various applied potentials and provide guidance for the design, testing, and in situ enhancement of compound materials for electrocatalysis.

3.1 Ex situ surface characterization of molybdenum nitride oxidation. For compound materials such as MoN, although ex situ characterization does not enable identification of the active site, it remains a valuable tool in developing materials of interest and serves as a baseline to understand and interpret in situ data. Thus, we have characterized the MoN catalyst surface after synthesis (< 1 week), substantial air exposure (~ 11 months), contact with electrolyte (~ 5 s at open circuit voltage (OCV)), and electrochemical testing (1 h chronoamperometry (CA) at 0.3 V vs RHE) (**Figure 1**, note: the acid dipped and 1 h CA samples were made from a sample kept under ambient conditions for 11 months) using XPS, ToF-SIMS, GI-XAS, and XRR.

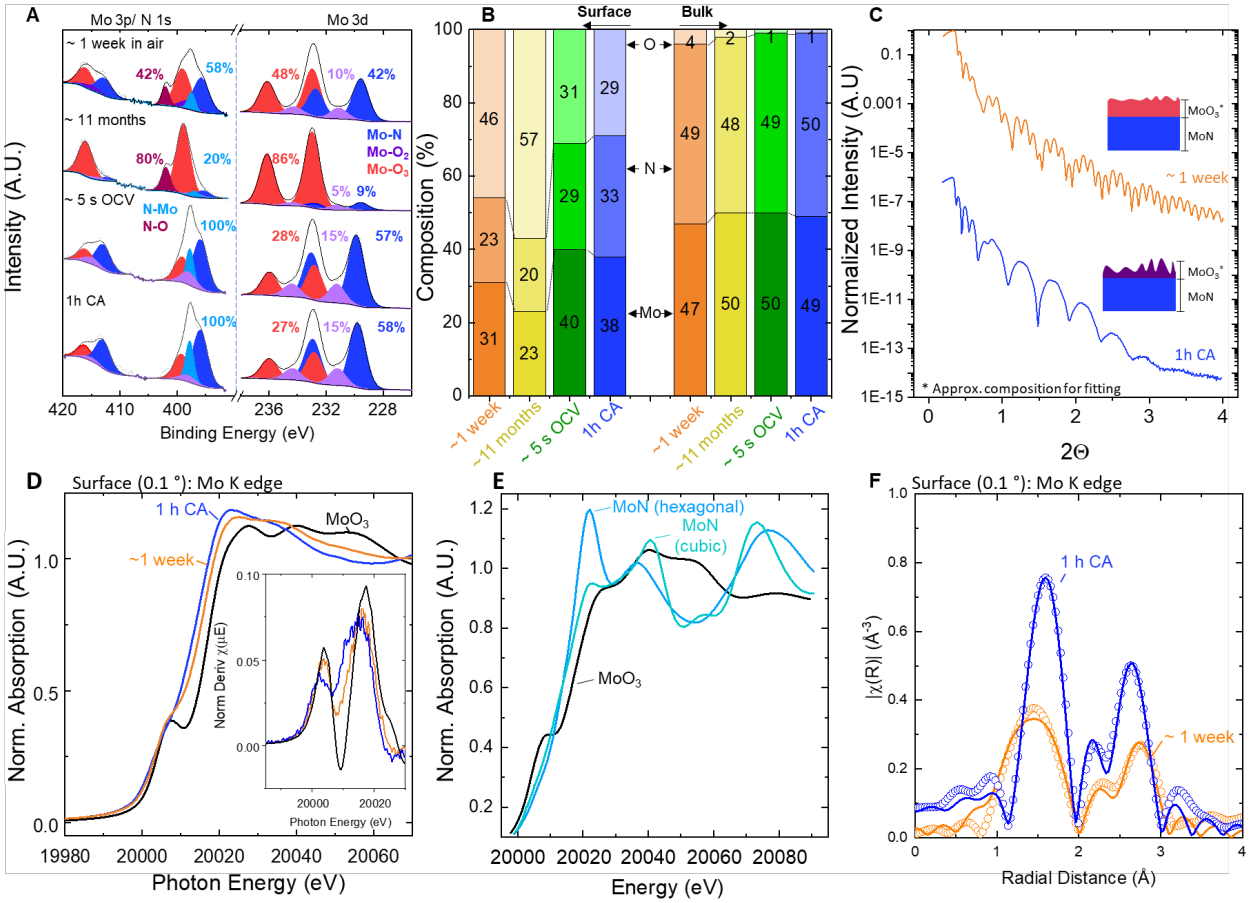

Figure 1. Ex situ surface and bulk compositional analysis of MoN films as-prepared (~1 week in air, orange), after 11 months in air (yellow), after ~ 5 s at OCV (green) in 0.1M $HClO_4$ electrolyte, and after a 1 h chronoamperometry stability test at 0.3 V vs RHE (1 hr CA, blue) via **(A)** XPS and **(B)** estimated surface (top ~ 5 nm) and bulk (at ~ 15 nm) compositions from combined XPS and ToF-SIMS analysis. **(C)** XRR patterns for the 1 week in air and 1 h CA films with schematics indicating changes in surface roughness and density. Fits for schematic models can be found in **Figure S2**. Mo K-edge **(D)** XANES, **(E)** simulated XANES for hexagonal MoN, cubic MoN, and MoO_3, and **(F)** EXAFS of MoN of the as-deposited and the 1 h CA films (surface, 0.1°, top ~ 3 – 5 nm)) with a MoO_3 reference. Inset in **(D)** show the first derivative of the normalized intensity. In **(F)**, data (circles) and fits (lines) are shown. Data from the 1 week in air sample in **(A)** and **(B)** have been reproduced with permission from ref (19) Copyright 2020 American Chemical Society.

Deconvolution of the Mo 3d, Mo 3p/N 1s, and O 1s XPS spectra shows significant variations in the ratio of surface (~ top 6 nm) Mo and N oxidation states depending on the treatment (**Figure 1A**). After 1 week of air exposure, the as-synthesized film shows a mixture of nitride and oxide character. Careful fitting allows for the identification of the Mo-N (229.6/232.7 eV), Mo-O_2 (231.1/234.2 eV), and Mo-O_3 (233.0/236.1 eV) contributions in the Mo 3d spectrum, which are

then used to deconvolute the overlapping Mo 3p/N 1s spectrum (**Figure S1**, **Table S1**). After storage under ambient conditions for 11 months, the surface of the Mo-N films substantially increases in O content. Mo is primarily present as an oxide and the fitted metal nitride peak at 397.0 eV accounts for only 20% of the total N area, with a larger peak corresponding to a nitrate species appearing at 402.0 eV. Probing the effect of electrolyte and electrocatalysis on the film surface, XPS on the 11-month air exposed films after ~ 5 s at OCV and a 1 h chronoamperometry (CA) measurement at 0.3 V vs RHE in 0.1 M $HClO_4$ shows a decrease in surface oxidation, below that of the 1 week film. The only N 1s peak is at 397.8 eV, but Mo-O_2 and Mo-O_3 peaks are still present in the Mo 3d spectra, suggesting that some oxide character remains during testing or re-forms in air.

The ToF-SIMS depth profiles and corresponding estimates of surface and bulk composition in **Figure 1B, S5** support the trend of surface oxidation increasing with air exposure and decreasing upon contact with electrolyte. Furthermore, depth profiling shows that while the bulk composition of the film does not change based on the treatment, the O content does decrease as a function of depth, reaching a steady state bulk concentration at ~ 5 nm, indicating the extent of O diffusion from air into the film. Interestingly, there is no change in Mo or N content as a function of depth, suggesting that O incorporation into the MoN creates an O-rich oxy-nitride layer rather than an oxide layer. The XRR analysis and fitting, as well as the depth resolved ToF-SIMS sputtering, indicate that the as-deposited (~ 1 week in air) film can be fit to a model with a total thickness of ~31.3 nm with the top 2.3 nm being a less dense MoO_3 with a roughness of 0.5 nm (**Figure 1C, S2**). It should be noted that while MoO_3 is used as an approximate composition for modeling purposes, the actual surface layer is likely an oxynitride, as shown by ToF-SIMs and XPS. XRR shows substantial increases in roughness (~8x increase with roughness of 3.5 nm) after the 5s OCV and 1 h CA treatments, indicating that the films are roughening and potentially thinning when in electrolyte. Furthermore, there is an observed decrease in sputtering time through the film in ToF-SIMS (**Figure S5**), which could support the film thinning/roughening conclusion from XRR. It should be noted, however, that the decrease in sputtering time could also be partially attributed to a drift (≤ 10%) in sputtering current during the measurement.

Ex situ Mo K-edge GI-XAS is used to probe the surface (0.1°) and bulk (5°) of the as-deposited (~ 1 week in air) and 1 h CA films. Mo K-edge x-ray absorption near edge structure (XANES)

(Figure 1D, see bulk GI-XAS in **Figure S6**) of the as-deposited film shows an increase in the pre-edge feature at the surface relative to the bulk. This peak increase typically corresponds with an increase in the forbidden 1s → 4d transition that becomes more allowed with increased distortion around the Mo atom and consequent p-d hybridization. While this feature does not provide a direct correlation to oxidation since there are Mo oxides (e.g. MoO_2) that do not exhibit this distortion, the similarity in position to the pre-edge peak measured for the MoO_3 reference powder supports the interpretation of this feature as a surface oxidation and O incorporation event. This is consistent with the surface oxidation as determined by XPS and ToF-SIMS. Furthermore, using FEFF9 to simulate XANES spectra for hexagonal and cubic MoN and MoO_3 we see that the distinctive pre-edge feature is only present for the MoO_3 structure (**Figure 1E**). While these representative structures help us identify the features in the spectra, future work using global optimization algorithms to predict stable oxynitride structures would be necessary to improve our understanding of the composition and coordination at the surface. Similarly, the edge position of the as-deposited film is higher than the 1 h CA film by ~ 3 eV, which further indicates a higher degree of oxidation, as found by XPS and ToF-SIMS. Finally, while it is difficult to distinguish between N and O atoms in XAS, in EXAFS we have fit the spectra using Mo-N and /or Mo-O paths from MoN and MoO_3 reference structures respectively, based on their distinct bond lengths (1.7 – 1.9 Å for MoO_3 and ~ 2.1 Å for MoN). Using this fitting schema, the best fits include a mix of Mo-N and Mo-O paths for both films, however, the Mo-O coordination is much lower in the 1 h CA film (**Figure 1F**, **Table S3**). Furthermore, its surface also has a smaller pre-edge feature in the XANES, indicating that a decrease in distortion correlates with less oxidation.

Together, the as deposited (~ 1 week and ~ 11 months), ~ 5 s OCV, and 1 h CA samples indicate that a surface (oxy)nitride layer grows in air but changes substantially in electrolyte or under ORR potentials, while the bulk of the film is stable. However, while the ~ 5 s OCV and 1 h CA films demonstrate a level of surface oxidation, it is impossible to know if the oxidation is due to electrolyte interaction, catalysis, or air exposure. Therefore, despite in depth, ex situ pre- and post-catalysis characterization, the structure and composition of the active surface during catalysis is convoluted by oxygen contamination in air and sensitivity to the electrolyte, making in situ compositional testing imperative.

3.2 Surface specific oxidation detected by in situ grazing incidence XAS. The surface of a catalyst under operating conditions is inherently dynamic, undergoing potential-dependent material transformations (e.g. redox, dissolution, composition changes) that impact catalyst longevity. As shown above (Section 2.1) and by others,[19,27,28,52] nitride materials, e.g. MoN, are particularly sensitive to both air and applied potential. To probe the MoN surface under ORR potentials (between 0 – 1.23 V vs RHE) and conditions (0.1 M $HClO_4$, O_2 bubbling), we developed a grazing incidence electrochemical cell (GI-cell) to study the dynamic surface composition and roughness using x-ray absorption and reflectivity, respectively. One important complication in studying catalyst surfaces in situ is distinguishing between the active material and the inactive core in the standard nanoparticulate configuration. Here, using a thin film model system, we can deconvolute the bulk and surface compositional components by changing the grazing angle of the incoming photon beam.

To date, there have only been a handful of studies probing the evolution of electrocatalyst surfaces under operating conditions via GI-XAS.[37–39] In this work, we have used a GI-cell to enable the study of small area thin films (< 1 cm_{geo}^2 area and < 100 nm thick) under applied potential. The replaceable sample mount allows for reuse of the cell, which employs a thin liquid overlayer (~ 100 μm) enclosed under a thin Kapton window (**Figure 2A**, **2B**, and **S7**). The surface and bulk of the catalyst film were studied by changing the GI angle between 0.1˚ (top ~3 nm) and 5.0˚ (all ~ 30 nm), respectively. It is important to note that spectra at very shallow grazing angles have significant contributions from x-ray self-absorption due to the shallow penetration depth and long pathlength into the sample.[53] Although it is difficult to correct for self-absorption effects in this configuration, it is still meaningful to quantitatively compare spectra at the same angle and to examine trends between angles.

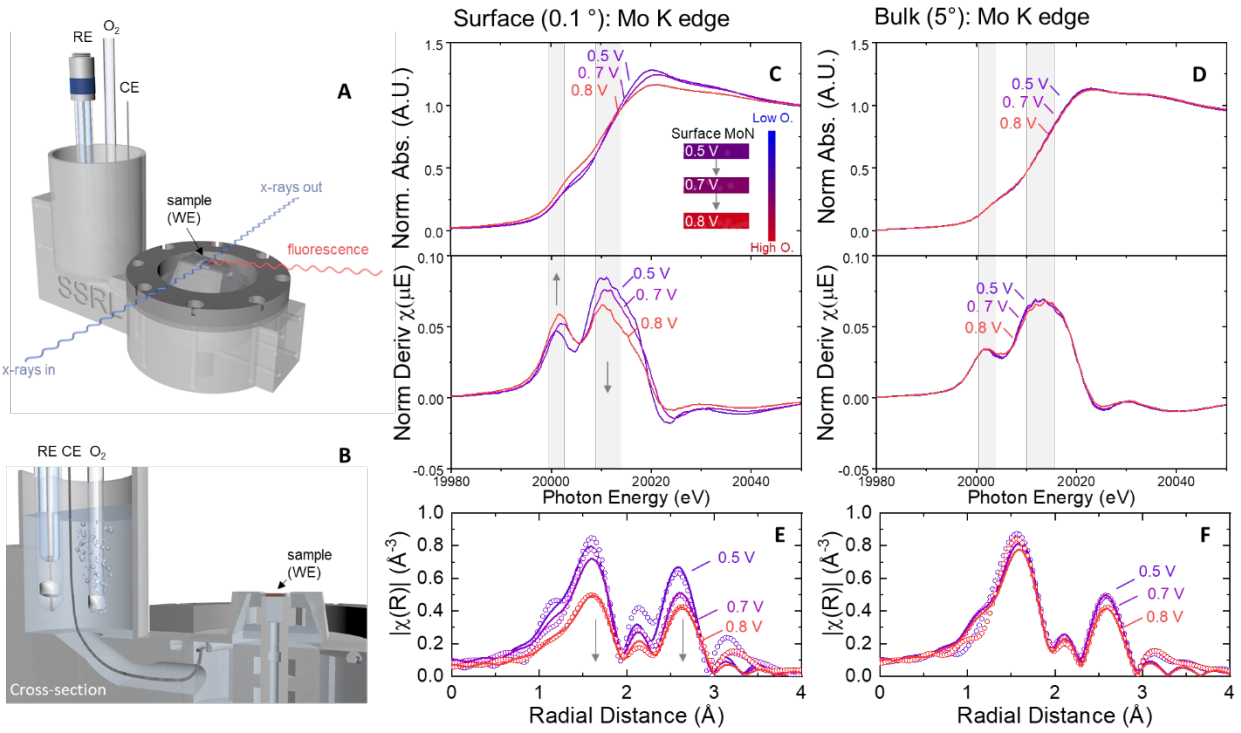

Figure 2. Schematics of the in situ GI-cell in **(A)** full and **(B)** in cross-section view. The Ag/AgCl reference, platinum wire, and sample are labeled RE, CE, and WE, respectively. The configuration of the beam and detector are indicated with arrows showing the paths of the x-rays and fluorescence from the sample. Total normalized absorption (top) and its first derivative (bottom) for the MoN film in O_2-bubbled 0.1 M $HClO_4$ at 0.5, 0.7, and 0.8 V vs RHE are displayed for **(C)** the surface (0.1˚) and **(D)** the bulk (5.0˚) with EXAFS and fits for the **(E)** surface and **(F)** bulk for the different potentials in situ with data indicated with circles and fits noted with lines. Shaded regions highlight the pre-edge and edge positions.

To probe the effect of applied potential on the catalyst surface, in situ XAS experiments were conducted nominally at 0.5, 0.7, and 0.8 V vs RHE looking at both the surface and bulk of the film in O_2-sparged 0.1 M $HClO_4$ electrolyte. After the in situ XAS experiments (~ 72 h), some beam damage to the film was observed in the form of a carbonaceous deposit on the surface of the film, as well as a slight reduction in the nominal Mo-N surface underneath this deposit, but no structural changes are apparent by surface sensitive GI-XRD (**Figure S8**). This carbon could be from the Kapton (polyimide polymer) that serves as the x-ray transparent window on top of our cell or the cell itself, which is made of plastic, that is slightly dissolved by the harsh acidic environment of our pH 1 electrolyte. However, over the course of the ~5 h experiment at each potential, there was minimal-to-no change in the spectra, and thus we believe this carbonaceous deposit was time-independent and therefore should not affect the potential dependent trends we observe. **Figure 2C**

shows the normalized intensity and first derivative of the surface XANES at the 3 potentials. Looking at the normalized intensity, we see that as the potential increases, the intensity of the pre-edge peak between 20,000.0 – 20,006.5 eV increases, the white line intensity decreases, and the edge position stays relatively constant. As stated previously, the pre-edge peak is an indicator of a distorted environment around the Mo atom which is present in the MoO_3 structure with distorted octahedral coordination. The pre-edge peak changes observed with increased potential are similar to the changes observed ex situ between the reduced (post 1h at 0.3 V vs RHE) and O rich (as-deposited, after ~ 1 week of air exposure) surfaces (**Figure 1**) in which the surface oxidation was established with XPS and ToF-SIMS characterization. Based on the observed correlation between XAS changes and known surface changes observed ex situ, we therefore hypothesize that the increase in pre-edge intensity indicates increased incorporation of O into the surface layer with increased potential (Figure **2C** inset schematic). Interestingly, a lack of substantial changes to the edge position indicates that the average Mo oxidation state is unchanged between 0.5 V to 0.8 V vs RHE, suggesting that the O incorporation does not impact the overall valence of the Mo. The other observed change, a decrease in the first peak white line intensity, has been associated with the allowed 1s-5p transition decreasing with distortion.

To further investigate any changes to the local structure of the films, analysis of the EXAFS region was performed. We fit the first two shells, excluding multiple scattering interactions, to possible Mo-(O/N) and Mo-Mo coordinations for each shell (**Figure 2E**). The spectra were fit using paths from FEFF9 generated from cif files for MoO_3 and MoN from the ICSD database.[50] The fits for each spectrum, including path length, coordination number, and edge energy, are detailed in the SI (**Figure S9-10**, **Table S4**). Due to self-absorption effects, which are exacerbated in the grazing incident geometry at low angles and are difficult to correct for, the fitted coordination numbers cannot be interpreted as absolute values. However, coordination numbers can be compared between the measurements taken at the same incidence angle. As previously stated, the film surface after several days of air exposure and prior to testing can be fit to a m+6ixture of Mo-N (from an MoN reference structure) and Mo-O (from an MoO_3 reference structure) in the first shell. At the first potential, 0.5 V vs RHE, XANES indicates that the surface is reduced (compared to the as-prepared spectrum) and the EXAFS is fit to only Mo-N coordination (**Figure 2E**). The Mo-N could be Mo coordinated to either N or O; however, we describe the fit as Mo-N because it does not include a path with a shorter bond (1.7 – 1.9 Å) associated with the MoO_3 structure. As the applied

potential is increased to 0.7 and 0.8 V vs RHE, the Mo-N and Mo-Mo bond lengths do not change substantially, but the coordination for both Mo-N and Mo-Mo decrease by ~ 1.7 and ~1.0, (between 0.5 V and 0.8 V) supporting the hypothesis of a particle size decrease along with surface amorphization during oxygen incorporation, respectively. Together, the XAS supports a surface model of an oxynitride layer that has a distorted local structure, shrinking particle size, and an increase in its amorphous nature with applied potential.

The bulk of the film (**Figure 2D)** behaves differently than the surface, with no discernible changes in the XANES with increased potential. Furthermore, EXAFS fitting shows small variations in coordination number and E_o but no clear trend with potential (**Figure 2E, Figure S11-12, Table S5**), indicating that the oxidation event that we see at low angles occurs primarily at the surface, and that, as in air, the oxy-nitride layer is self-passivating at potentials between 0.5 - 0.8 V vs. RHE. However, it is important to note that the edge position of the bulk is higher than the edge position of the surface at every potential. This could indicate that the bulk is more oxidized than the surface. However, because the surface has slight beam damage and is more impacted by self-absorption, we believe that the absolute values of the surface and bulk are not directly comparable, and thus we focus only on trends between surface and bulk. Having established the existence of potential-dependent surface changes with a stable bulk composition, it is important to understand how this amorphized oxynitride surface layer changes affect electrochemical performance.

3.3 Activity and stability tuned as a function of applied potential. For well-explored catalyst systems, such as Pt-based catalysts for ORR, potential cycling or conditioning protocols have been established to activate the catalyst and thereby extract the maximum performance.[54] Development of optimal conditioning and testing procedures for new catalysts is non-trivial because it requires extensive understanding of the electrochemical behavior and active site of the catalyst. Redox sensitive non-noble transition metal-based materials (e.g. those with several stable oxidation states, such as Mo) are especially complicated to study due to the large phase space of active site compositions. Based on GI-XAS measurements (Section 2.2), we have demonstrated that the surface of MoN incorporates O with increasing potentials. To probe the role of applied potential and compositional change on electrochemical activity, surface area, and stability, studies using a rotating disk electrode (RDE) for efficient mass transport were performed, wherein the catalyst

was placed into the electrolyte (0.1 M $HClO_4$) under potential control (at 0.05 V vs RHE) and then was assessed using the CV testing protocol (**Figure 3A**). Under this protocol, CVs (two cycles) were conducted in four potential windows (0.05 – 0.3, 0.05 – 0.5, 0.05 – 0.7, and 0.05 – 0.8 V vs RHE) in O_2-saturated electrolyte, and the change in overpotential at a specific current density was measured (**Figure 3B**). A separate sample was tested in the same potential windows in N_2-saturated electrolyte at different scan rates, allowing for determination of the change in the electrochemical double layer capacitance (EDLC) at 0.3 V vs RHE (**Figure 3C, Figure S13**).

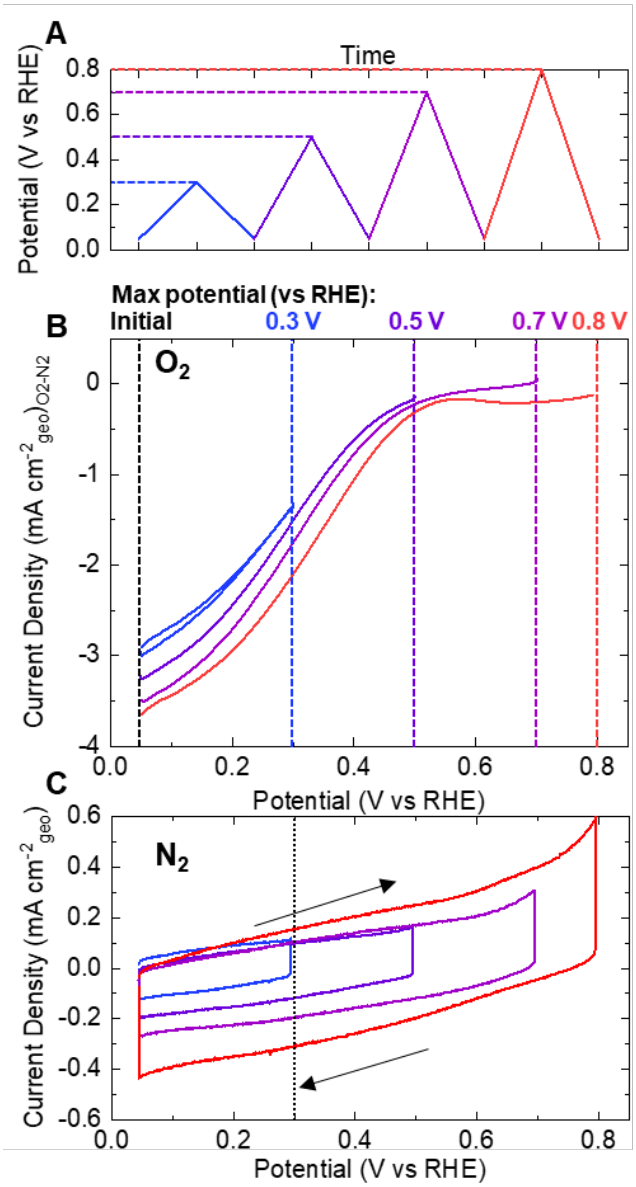

Figure 3. Electrochemical potential cycling measurements on a glassy carbon electrode in RRDE at 20 mV s^{-1} and 1600 rpm. **(A)** Cycling protocol for the 0.05 – 0.3 (blue), 0.05 – 0.5 (purple), 0.05

– 0.7 (light purple), and 0.05 – 0.8 (red) V vs RHE sweeps. **(B)** ORR cyclic voltammograms in O_2-saturated 0.1 M $HClO_4$ with increasing maximum potential; for clarity, the reverse sweep only is shown for the 0.5 - 0.8 V RHE cycles. **(C)** Capacitance cyclic voltammograms in N_2-saturated 0.1M $HClO_4$ with increasing maximum potential. Dashed line indicates the potential (0.3 V vs RHE) at which the EDLC was evaluated.

On a geometric current density basis, the overpotential for oxygen reduction at -2 mA cm_{geo}^{-2} decreases by ~ 30 , 25, and 35 mV when cycled to 0.5, 0.7, and 0.8 V vs RHE, respectively (**Figure 3B**). This amounts to a total ORR activity improvement of ~ 90 mV with potential cycling. **Figure 3C** shows the same cycling study in N_2-saturated electrolyte, which allows us to probe non-catalytic, electrochemical changes that occur at these potentials. Notably, the anodic current shows very little change for any of the cycles within the range of 0.3 - 0.7 V vs RHE; however at 0.8 V vs RHE, there is a substantial increase. The cathodic current shows a different trend as it steadily increases with an increase in maximum potential for each of the potential ranges investigated. Evaluation of the $EDLC_{anodic}$ and $EDLC_{cathodic}$ at 0.3 V vs RHE for each potential range (**Figure 4A**), shows the same trend: small changes in anodic and large increases in cathodic capacitance, the latter of which is potentially convoluted with ORR current if reduction of O from the lattice occurs. For this reason, we base our analysis on the anodic contribution, which at this potential should not have any convoluting Faradaic currents. Generally, changes in EDLC could indicate changes in electrochemical surface area (ex. by roughening or increasing porosity), specific capacitance (ex. oxide/oxynitride vs nitride), or a combination of these effects.

To disentangle these effects and determine the root of the performance enhancement, we also monitored the in situ morphology (**Figure 4B**, XRR) and Mo dissolution (**Figure 4C**, ICP-OES see **Figure S14** for CA profiles) as a function of potential. While the dissolution and morphology measurements are done in different cells (RDE vs GI-cell) and the mass transport and total current densities are different, they both indicate that at potentials $\leq$ 0.7 V vs RHE the MoN does not significantly dissolve or roughen. However, after ~ 5 h of polarization at 0.8 V vs RHE, the MoN dissolves entirely in an RDE cell and the density decreases significantly by XRR in the GI-cell configuration. While a surface area measurement from EDLC for this type of material is complicated to interpret, because the intrinsic capacity could change with composition, the conservation of this current enhancement, along with the Mo stability and the lack of discernible

roughness changes (≤ 0.7 V vs RHE), indicates that the incorporation of O into the surface is generally enhancing the intrinsic activity of the MoN. Interestingly, if normalized by $EDLC_{anodic}$ we still see an enhancement of ~ 95 mV at -4 mA mF_{EDLC}^{-1} between 0.3 V and 0.7 V vs RHE (**Figure S15**). However, at 0.8 V vs RHE and above, the performance enhancement is likely due to roughening caused by dissolution that increases the number of active sites electrochemically available on the surface. It is also possible that the intrinsic activity of sites is changing, however it is difficult to disentangle intrinsic active-site changes from performance changes due to roughening. The stability of this system was further probed by performing 30 cycles in each potential range (**Figure S14**). Below 0.7 V vs RHE, the performance was stable within each range and the activity trend was not impacted by extended cycling. Upon increased cycling to 0.8 V vs RHE, the oxidation feature grew and the performance continued to increase, consistent with continual roughening. This indicates that while we can continue to incorporate O into the surface with increased polarization, there is a stability trade off.

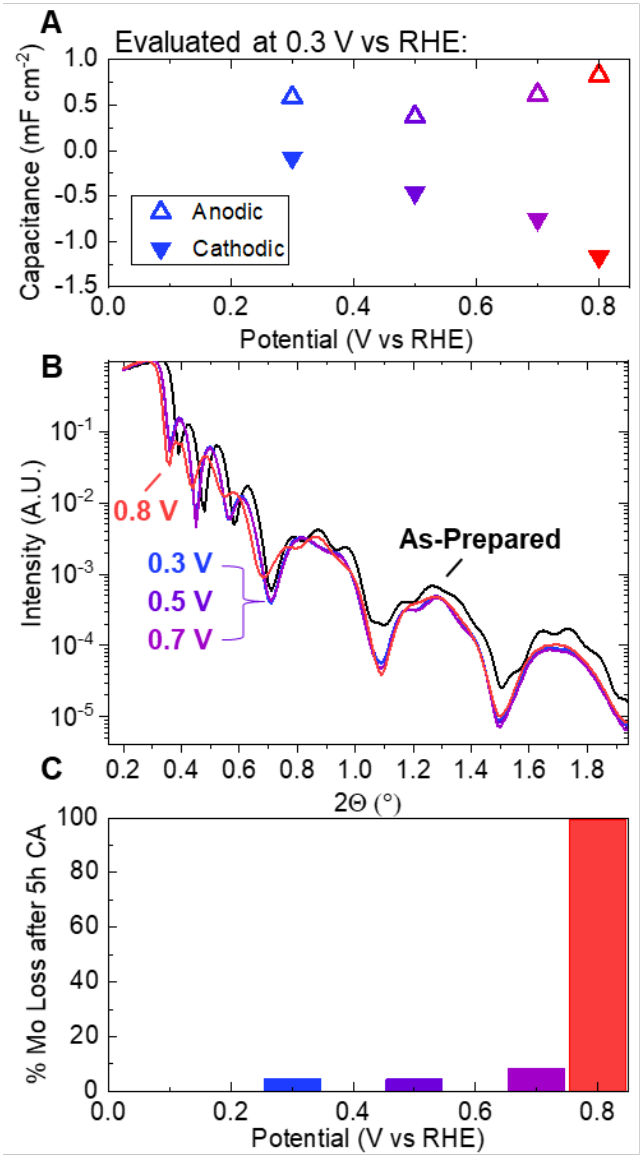

Figure 4. (A) Anodic (empty) and cathodic (filled) EDLC at 0.3 V vs RHE after exposure to different maximum potentials based on the cyclic voltammograms on glassy carbon electrodes in the RRDE in N_2-saturated 0.1M $HClO_4$ in **Figure 3C**. **(B)** In situ XRR measurements on catalyst on Si substrate in the GI-cell at 0.3. 0.5, 0.7, and 0.8 V vs RHE compared with an ex situ measurement of the as-prepared film. **(C)** ICP-OES stability measurements on rotating Si electrodes at 0.3, 0.5, 0.7, and 0.8 V vs RHE.

We further observe a greater potential dependence (on a geometric basis) for films with longer air exposure and an increase in H_2O selectivity with increased max potential cycling. ORR activity selectivity data collected using a rotating ring disc electrode (RRDE) can be found in **Figure S16**. In particular, after ~ 1 month in air, the overpotential to reach -2 mA cm_{geo}^{-2} increased by 130 mV

in the 0.05 – 0.3 V vs RHE cycle, compared to the pristine sample. This deactivation suggests that the air-O rich surface is less active for ORR. However, after cycling to 0.8 V vs RHE, the activity overlays with that of films that were not previously exposed to air, indicating that the surface has been effectively cleaned and reactivated. This likely indicates that the O rich surface layer formed in air is different than the layer formed electrochemically. From a practical perspective, understanding how activity is impacted and can be recovered with catalyst storage is very useful. Taken together, the potential-dependent activity and stability suggest that the catalyst surface varies greatly with applied potential. To further understand why cycling to higher potentials improves ORR activity, it is necessary to understand the stability of the compositional and/or structural changes occurred during potential cycling.

3.4 Oxynitride surface stability under ORR relevant potentials. To further understand the role that the oxynitride surface plays in enhancing performance, it is necessary to determine the stability of the surface under ORR relevant conditions. Previous RDE studies under well-controlled O_2 mass transport conditions show these MoN thin films have an ORR onset potential of ~ 0.56 V vs RHE at -0.1 mA cm^{-2}.[19] Therefore, we consider all potentials < 0.6 V vs RHE in this study to be *ORR relevant.* Using GI-XAS, we probe the ORR stability of the surface by applying a sequence of gradually increasing potentials from 0.5 V to 0.9 V vs RHE and returning to 0.3 V vs RHE between each step. **Figure 5** shows the experimental sequence, XANES, and EXAFS with fits comparing each 0.3 V step to its previous condition. Details and tabulation of fits can be found in **Figures S9-10** and **Table S4**.

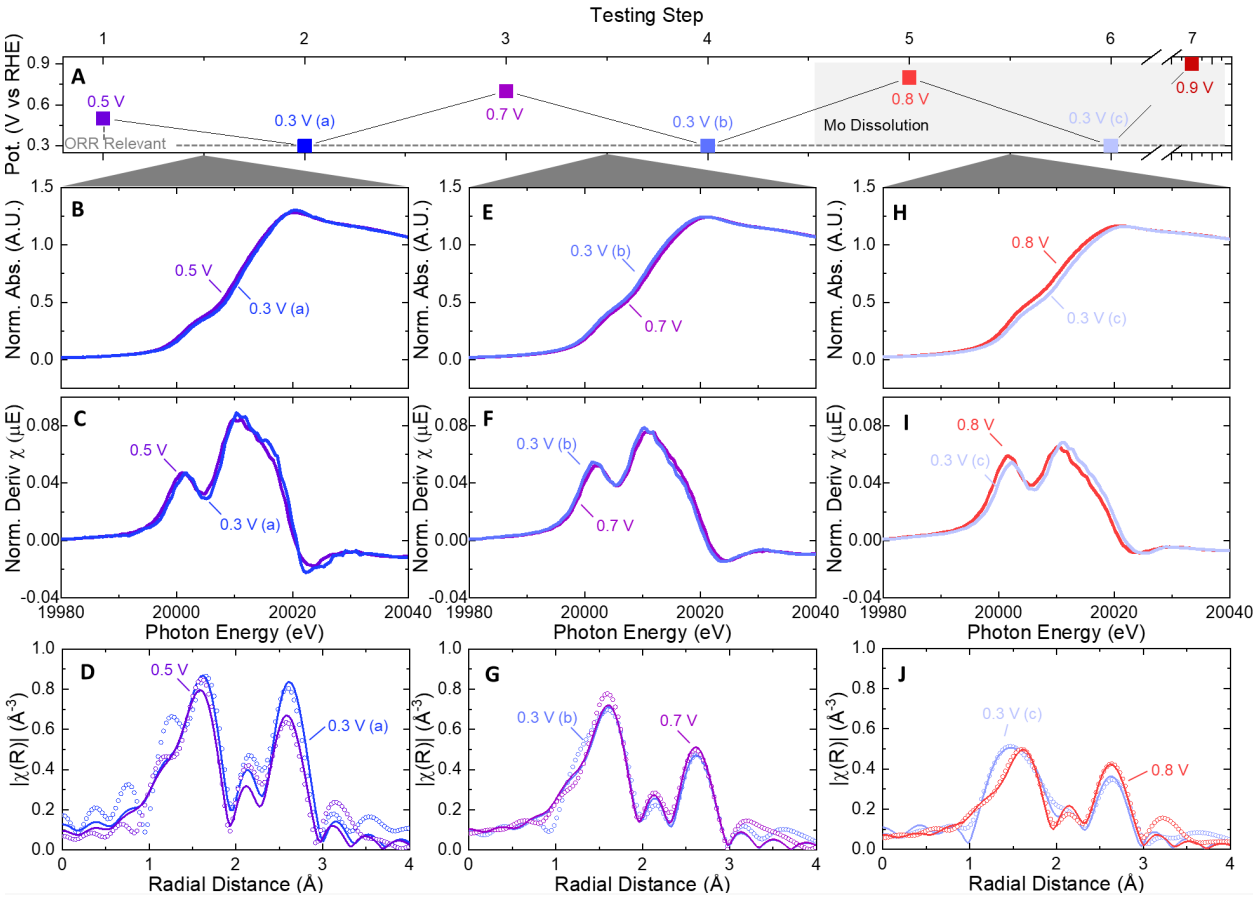

Figure 5. In situ GI-XAS of the surface of the MoN film with O_2-bubbled in 0.1 M $HClO_4$ at a series of different potentials in a specific (**A**) testing order. ORR relevant potentials 0.5 V and 0.3 V vs RHE and dissolution potential 0.8 V vs RHE are noted with dotted lines and a grey box respectively. The normalized absorption, its first derivative, and the EXAFS with fits are shown for three potential sequences comparing (**B-D**) 0.5 V and 0.3 V (a), (**E-G**) 0.7 V and 0.3 V (b), and (**H-J**). See **Figures S12-14** for XAS spectra and tabulated and graphed fitting values **Tables S2-4.**

Comparing the polarization at 0.5 V to its subsequent polarization at 0.3 V (a) (where lettering a, b, etc. is used to denote the testing order), we see that there is little change in the XANES profile and from EXAFS there are negligible changes in bond lengths and coordination numbers for Mo-N or Mo-Mo (**Figure 5 B-D**). This lack of change in local structure and oxidation state indicates that the surface of the film is largely the same at both ORR relevant potentials of 0.5 V and 0.3 V vs RHE. After this first sequence, the second sequence is at 0.7 V and 0.3 V (b) vs RHE polarization (**Figure 5 E-G**). With the increased polarization at 0.7 V vs RHE, as noted in section 3.2, O is incorporated into the surface of the film, the surface becomes more amorphous, and the surface particle size shrinks. When this oxynitride layer is polarized at 0.3 V (b) vs RHE we see

that it is largely stable and there are no discernable differences either in XANES or EXAFS. Finally, in the third sequence the film is polarized at 0.8 V and then at 0.3 V (c) vs RHE (**Figure 5 H-J**). As shown by XRR and ICP-OES (Section 3.3), 0.8 V vs RHE is the potential at which the Mo begins to dissolve and the surface roughens. It is therefore interesting to observe that the surface at 0.3 V (c) is substantially different from that at 0.8 V vs RHE, as seen by the main edge energy shift in XANES and peak shift / growth in EXAFS. In fact, 0.3 V (c) is the only in situ surface in testing steps 1 – 6 that is fit with both a Mo-N and Mo-O path, indicating that substantial chemical changes are occurring at the surface. It is important to note that the MoN film conditioned in this manner at 0.8 V vs RHE has the highest ORR performance (**Figure 3**) suggesting a relationship between activity and the O content, amorphization, and roughness of the surface. The observed O-rich surface at 0.3 V (c) could be due stabilization of the surface oxynitride (that grew, but slowly dissolved at 0.8 V) or simply to a larger area of O incorporated film surface due to roughening.

To summarize, our in situ measurements show that the film incorporates O and becomes more amorphous when exposed to high potentials, and that these potential-dependent surface changes remain or are increased (as in the case of the 0.8 V conditioning) when the film is returned to an ORR-relevant potential. This provides the first evidence that this surface oxynitride layer is stable on molybdenum nitride at ORR conditions on an extended time scale (~ 5 h).

Compared to the surface of the film, the bulk displays minimal changes with applied potentials ≤ 0.8 V vs RHE. In fact, the coordination numbers and atomic distances for Mo-N and Mo-Mo remain very similar to the ex situ samples (**Figure S15**). Features observed for the bulk of the film measured at 0.9 V vs RHE are dramatically different from those measured in the 0.3 – 0.8 V vs RHE range. Compared to the 0.5 V film, we see substantial changes in the XANES (**Figure 6A**) and EXAFS (**Figure 6B**). Between these potentials, the edge energy increases by ~5.5 eV and the pre-edge intensity increases by ~0.02, corresponding to increased oxidation of the entire film. In particular, the increase in EXAFS signal at low radial distance indicates the significant present of MoO_3-like Mo coordination in the bulk of the film. We have therefore demonstrated that it is possible to change the bulk of the film through application of highly oxidizing potentials.

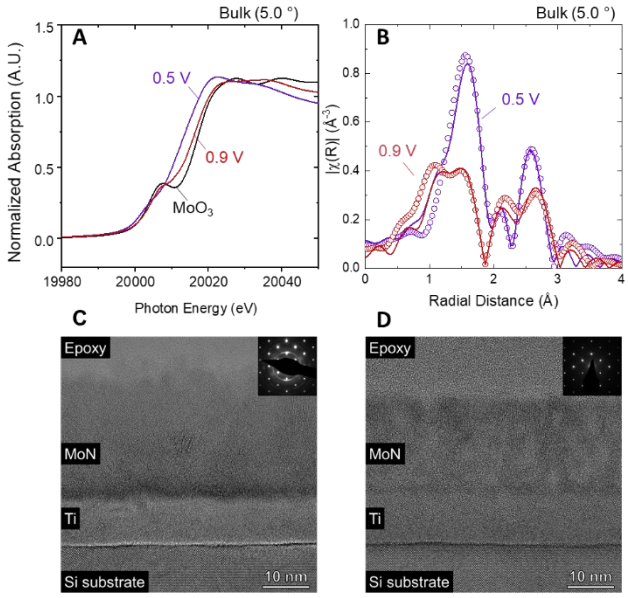

Figure 6. Bulk (5.0 °) **(A)** XANES and **(B)** EXAFS of the Mo K-edge at 0.5 V and 0.9 V vs RHE. The EXAFS is displayed with the data (circles) and fits (lines) in R-space. High resolution cross-sectional TEM images of the MoN film **(C)** as-synthesized and **(D)** post x-ray in situ analysis. Insets show SADPs taken over the regions of both Si substrate and thin film; both show spots corresponding to the [110] zone axis of Si, while rings corresponding to polycrystalline Mo_2N are observed in the **(C)** only. The TEM image and SADP in **(C)** have reproduced with permission from ref (19) Copyright 2020 American Chemical Society.

In addition to in situ characterization of the film structure and oxidation state, it is also important to understand the stability of the film morphology. Characterization of the film after oxidation above 0.8 V vs RHE is particularly interesting, as this is where ICP and XRR show that the film begins to dissolve and roughen (**Figure 3B** and **C**). Given that significant differences in cell geometry and current densities exist between the RDE and the GI-cell, we anticipate that the dissolution rate of the Mo-N film will be lower in the GI-cell. As an approximation of material lost, in situ XRR indicates that the film thickness and roughness remain unchanged until the 0.8 V vs RHE potential, at which point the film begins to roughen (**Figure 4B and C**). Therefore, we hypothesize that as the film incorporates O and becomes more amorphous at potentials ≥ 0.8 V vs RHE, it also slowly dissolves, removing portions of the high O content layer and exposing more active sites to the electrolyte that are then available during ORR. Cross-sectional HR-TEM, SADP, and STEM-EDS mapping of the sample after GI-XAS studies (**Figure 6C-D** and **S17**) supports these conclusions. In comparison with the pre-test sample, the film has thinned from ~28 nm to 21

nm and the elemental density is low. Furthermore, the MoN diffraction rings visible in the SADP in the pre-test sample are no longer present after testing, indicating that the film has become amorphous, as was observed by GI-XAS. Together, these data suggest that at potentials below 0.8 V vs RHE, the performance enhancement is due to a stable amorphous O rich surface layer, but at potentials ≥ 0.8 V vs RHE, further enhancements likely arise from Mo-dissolution and surface roughening that expose more active sites.

3.5 Theoretical study of potential-driven O incorporation. Given the potential-dependent surface composition and ORR activity of MoN, it is useful to investigate the conditions that give rise to these changes. Specifically, determining the electrochemical potentials at which surface oxidation and dissolution become thermodynamically favorable can provide insight into the kinetic barriers for these processes by comparison to experimental values. For instance, if oxidation is observed at a significantly higher potential than that at which oxidized MoN or MoO_x become thermodynamically favorable, then this may indicate a significant kinetic barrier for this process. A high kinetic barrier may in turn reflect a significant degree of surface reorganization or structural changes associated with oxidation.

Pourbaix diagrams are commonly used to describe the relative thermodynamic stability of multiple species within an aqueous system.[47] By representing the most stable combination of species at varying pH and electrochemical potentials, these diagrams provide an estimate of the potential and pH at which phase transformations become thermodynamically favorable.[add dynamic Pourbaix refs here?] Pourbaix diagrams are constructed based on the formation free energy of each phase within a system, and computational methods like DFT can be employed to estimate these values for a wide range of species. **Figure 7A** shows the theoretical Pourbaix diagram for the Mo-N aqueous system constructed according to the computational methods detailed in the Experimental section. In addition to the regions of stability for each combination of stable phases within Pourbaix space, **Figure 7B** shows the decomposition free energy (ΔG_{pbx}) of hexagonal MoN. ΔG_{pbx} is defined according to Equation 1 below, where G_{MoN} is the free energy of MoN and G_{stable} is the free energy of the most stable species at a given potential and pH in Pourbaix diagram.[48]

$$\Delta G_{pbx} = G_{MoN} - G_{stable} \quad (1)$$

By definition, a thermodynamic stable phase has a ΔG_{pbx} value of zero. Compounds with larger ΔG_{pbx} values are less stable. Previous theoretical Pourbaix studies suggest that metastable species may exist in aqueous systems with ΔG_{pbx} up to 0.5 eV/atom due to high solid-solid phase transformation barriers or the formation of passivation layers at the surface.[55] [or here?] Within the Mo-N-O-H system, hexagonal MoN surpasses the 0.5 eV/atom threshold above 0.2 V vs RHE at pH 1, suggesting that this phase may be metastable below this potential. At increasingly oxidative potentials, the large ΔG_{pbx} (1.2 eV/atom at 0.8 V) indicates that there is a strong thermodynamic driving force for MoN to decompose. The most stable Mo-containing species at pH 1 is MoO_2 at 0.3 - 0.5 V_{SHE} and $MoO_3 \cdot 2H_2O$ at higher potentials. The increasing oxidation state of Mo within the most stable species at oxidizing potentials aligns with the experimentally observed increase in the pre-edge peak intensity from GI-XAS in **Figure 5A**.

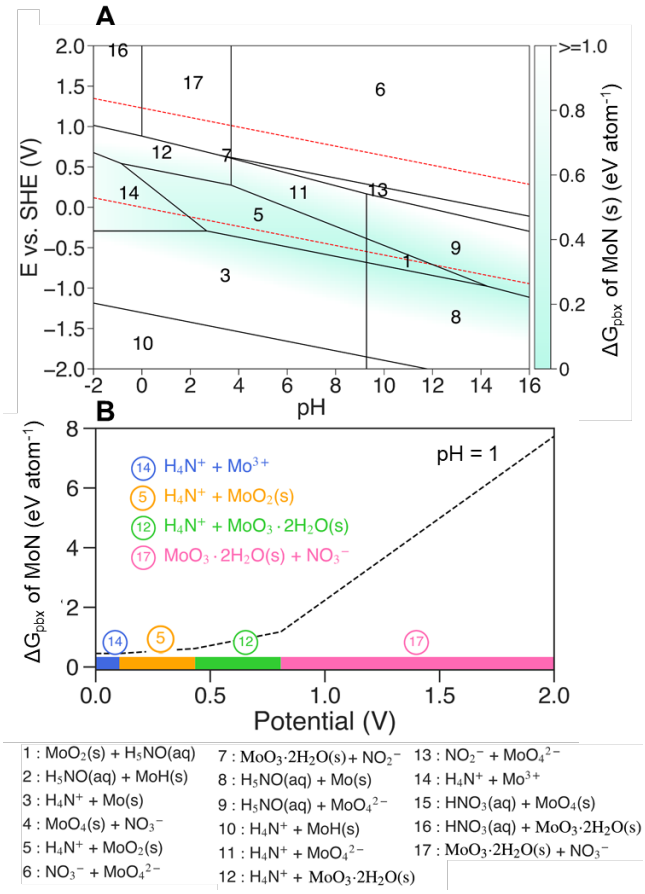

Figure 7. (A) Calculated Mo-N-O-H Pourbaix diagram generated with aqueous ion concentration of 10^{-6} M at 25 °C. The shaded area in blue represents the calculated Pourbaix decomposition free energy (ΔG_{pbx}). A higher ΔG_{pbx} indicates a less stable species. Reactions on the right panel show

the aqueous decomposition products labeled in the corresponding regions in the Pourbaix diagram. The water stability window is shown in red dashed lines. **(B)** ΔG_{pbx} of MoN as a function of potential from 0 - 2.0 V vs SHE at pH = 1. The projection of ΔG_{pbx} onto the potential axis highlights the stable species in the corresponding regions.

While Pourbaix analysis provides insight into the relative stability of pristine bulk phases within the Mo-N-O-H system, it is also useful to understand the energetics of O incorporation into defects, which we have previously observed in the experimentally synthesized MoN.[19] To that end, we calculated the differential formation energies of O substitution into N vacancies within otherwise pristine cubic and hexagonal MoN bulk structures under different conditions. Equations 2 and 3 represent the O substitution equation under ambient conditions and reaction conditions, respectively. The energies of these reactions, represented by ΔG_{air} and ΔG_{aq} respectively, were computed via DFT. We employed the computational hydrogen electrode (equation (4)) to represent the energy of the protons and electrons under reaction conditions.

$$Mo_nN_{n-1} + \frac{1}{2}O_2 \rightarrow Mo_nN_{n-1}O \quad (2)$$

$$Mo_nN_{n-1} + H_2O \rightarrow Mo_nN_{n-1}O + 2H^+ + 2e^- \quad (3)$$

$$H_2 \rightarrow 2H^+ + 2e^- \qquad \Delta G = 0 \text{ eV at 0 V vs. RHE} \quad (4)$$

We considered both pristine and O-substituted cubic and hexagonal MoN structures to reflect the bulk composition of the structures studied experimentally. Note that the influence of varying O substitution and N vacancy concentrations on the formation energies of these structures has been previously investigated, and a similar analysis can be applied to any of these systems.[19] For the pristine bulk structures, the ΔG_{aq} and voltage at which O substitution becomes favorable are shown in **Table S6**. The results indicate that O substitution is thermodynamically favorable under both ambient conditions and potentials above ~0.5 V vs. RHE in aqueous conditions. However, this process is unfavorable at 0 V vs. RHE, which agrees with our experimental results that do not show significant bulk O incorporation into MoN at low potentials (**Figure S12).** Collectively, our

results show an increasing thermodynamic driving force for MoN oxidation at increasing ORR potentials.

4.0 Conclusion

To uncover the stable oxynitride in situ surface of the MoN catalyst, we combined in situ GI-XAS and XRR with complementary electrochemical, mass dissolution, and theoretical analysis. We find that the O rich surface layer that grows in air is removed quickly after any contact with electrolyte. Notably, an O rich surface layer can be re-grown in situ with the application of increasingly oxidizing potentials. Between 0.3 V and 0.7 V vs RHE, this oxidation and amorphization coincides with increased activity, and in situ XRR and ex situ ICP indicate that the film does not roughen or dissolve in this range. Above 0.7 V vs RHE, however, while we continue to observe surface oxidation, it is concurrent with substantial Mo dissolution and roughening, indicating that the observed performance enhancement is a result of both increasing surface area and surface oxidation. Calculated Pourbaix analysis reveals that metastability of MoN under ORR conditions may be attributed to high solid-solid phase transformation barriers. This extensive analysis of the catalyst surface provides insight into the effects of potential conditioning and how this may be leveraged to design new catalysts in situ. With a clear understanding of not only the performance response, but also the mechanism behind these changes, e.g. composition change, degradation, and/or roughening, this platform for in situ testing could be used to tune desired material properties and lead to the stabilization of new phases of highly efficient materials that are not air stable.

Summary of Supporting Information

Additional materials characterization (XPS, XRR, XRD, ToF-SIMS, TEM), electrochemical measurements, and details of GI-XAS fitting parameters and results.

Author Contributions

M.B.S and M.E.K contributed equally.

Notes

The authors declare no competing financial interest.

Acknowledgments

This work was supported by the Toyota Research Institute. Part of this work was performed at the Stanford Nano Shared Facilities (SNSF) and the Stanford Nanofabrication Facility (SNF), supported by the National Science Foundation under Award ECCS-1542152. Use of the Stanford Synchrotron Radiation Lightsource, SLAC National Accelerator Laboratory, is supported by the U.S. DoE, Office of BES under Contract No. DE-AC02-76SF00515. Part of this research (ToF-SIMS characterization) was conducted at the Center for Nanophase Materials Sciences, which is a DOE Office of Science User Facility, using instrumentation within ORNL's Materials Characterization Core provided by UT-Battelle, LLC under Contract No. DE-AC05-00OR22725 with the U.S. DoE. The authors thank Guanchao Li in the Stanford Environmental Measurements Facility for the acquisition of ICP-MS and OES data. Authors MEK and MBS would like to thank Alan Landers for insightful discussions. The authors thank Melissa Wette and Drew Higgins for their work in developing the GI-cell. Author AP thanks the National Science Foundation Graduate Research Fellowship Program (NSF GRFP).

References

(1) Song, C.; Zhang, J. PEM Fuel Cell Electrocatalysts and Catalyst Layers: Fundamentals and Applications; Zhang, J., Eds.; Vancouver, BC, 2008; pp 89-129.

(2) Publication Office of the European Union, Hydrogen Roadmap: A Sustainable Pathway for the European Energy Transition. Europe. https://doi.org/10.2843/249013 (accessed Sept. 29, 2020)

(3) Staffell, I.; Scamman, D.; Velazquez Abad, A.; Balcombe, P.; Dodds, P. E.; Ekins, P.; Shah, N.; Ward, K. R. The Role of Hydrogen and Fuel Cells in the Global Energy System. *Energy Environ. Sci.* **2019**, *12*, 463–491.

(4) Hydrogen Council, Path to Hydrogen Competitiveness: A Cost Perspective. https://hydrogencouncil.com/ (accessed Sept. 29, 2020).

(5) Argonne National Laboratory, GREET® Model The Greenhouse gases, Regulated Emissions, and Energy use in Transportation Model. https://greet.es.anl.gov/ (accessed Sept. 29, 2020).

(6) Yazdanie, M.; Noembrini, F.; Dossetto, L.; Boulouchos, K. A Comparative Analysis of Well-to-Wheel Primary Energy Demand and Greenhouse Gas Emissions for the Operation of

Alternative and Conventional Vehicles in Switzerland , Considering Various Energy Carrier Production Pathways. *J. Power Sources* **2014**, *249*, 333–348.

(7) Argonne National Laboratory. Fuel Well-to-Wheels Analysis of Energy use and Greenhouse Gas Emissions of Plug-In Hybrid Electric Vehicles. https://www.energy.gov/sites/prod/files/2014/03/f9/67242.pdf (accessed Sept. 29, 2020).

(8) Sui, S.; Wang, X.; Zhou, X.; Su, Y.; Riffat, S.; Liu, C. A Comprehensive Review of Pt Electrocatalysts for the Oxygen Reduction Reaction: Nanostructure, Activity, Mechanism and Carbon Support in PEM Fuel Cells. *J. Mater. Chem*. *A* **2017**, *5*, 1808–1825.

(9) Gomez-Marin, A. M.; Rizo, R.; Feliu, J. M. Oxygen Reduction Reaction at Pt Single Crystals : A Critical Overview. *Catal. Sci. Technol*. **2014**, *4*, 1685–1698.

(10) Casalongue, H. S.; Kaya, S.; Viswanathan, V.; Miller, D. J.; Friebel, D.; Hansen, H. A.; Nørskov, J. K.; Nilsson, A.; Ogasawara, H. Direct Observation of the Oxygenated Species during Oxygen Reduction on a Platinum Fuel Cell Cathode. *Nat. Commun*. **2013**, *4*, 1-6.

(11) Ramaswamy, N.; Mukerjee, S. Fundamental Mechanistic Understanding of Electrocatalysis of Oxygen Reduction on Pt and Non-Pt Surfaces: Acid versus Alkaline Media. *Adv. Phys. Chem*. **2012**, *2012*, 1-17.

(12) Kato, H. In-Situ Liquid TEM Study on the Degradation Mechanism of Fuel Cell Catalysts. *SAE Int.J. Alt. Power,* **2016**, *5,* 189–194.

(13) Mizutani, N.; Ishibashi, K. Enhancing PtCo Electrode Catalyst Performance for Fuel Cell Vehicle Application. *SAE Int.* **2016**, *1187*, 1–5.

(14) Ganesan, A.; Narayanasamy, M. Ultra - Low Loading of Platinum in Proton Exchange Membrane - Based Fuel Cells : A Brief Review. *Mater. Renew. Sustain. Energy* **2019**, *8*, 1–14.

(15) US Department of Energy (DOE). Multi-Year Research, Development, and Demonstration Plan: 3.4 Fuel Cells. https://doi.org/Department of Energy (accessed Sept. 29, 2020).

(16) Alexander, A.; Hargreaves, J. S. J.; Alexander, A.; Alexander, A.; Joyner, R. Alternative Catalytic Materials : Carbides , Nitrides , Phosphides and Amorphous Boron Alloys. *Chem. Soc. Rev.* **2010**, *39*, 4388–4401.

(17) Chisaka, M. Transition Metal Oxide, Oxynitride, and Nitride Electrocatalysts with and without Supports for Polymer Electrolyte Fuel Cell Cathodes 14.2 Transition Metal Oxide and Oxynitride Electrocatalysts; Maiyalagan, T., Saji, V., Eds.; WILEY-VCH Verlag, 2017; pp. 423 – 441.

(18) Farakas, N.; Tokash, J.C.; Zhang, G.; Evans, E.A.; Ramsier, R.D.; Dagata, J. A. Local Oxidation of Metal and Metal Nitride Films. *J. Vac. Sci. Technol. A* **2004**, *22*, 1879–1884.

(19) Kreider, M. E.; Stevens, M. B.; Liu, Y.; Patel, A. M.; Statt, M. J.; Gibbons, B. M.; Gallo, A.; Ben-naim, M.; Mehta, A.; Davis, R. C.; et al. Nitride or Oxynitride ? Elucidating the

Composition − Activity Relationships in Molybdenum Nitride Electrocatalysts for the Oxygen Reduction Reaction. *Chem. Mater.* **2020**, *37*, 2946–2960.

(20) Abroshan, H.; Bothra, P.; Back, S.; Kulkarni, A.; Nørskov, J. K.; Siahrostami, S. Ultrathin Cobalt Oxide Overlayer Promotes Catalytic Activity of Cobalt Nitride for the Oxygen Reduction Reaction. *J. Phys. Chem. C.* **2018**, *122*, 4783-4791.

(21) Schulenburg, H.; Stankov, S.; Schu, V.; Dorbandt, I.; Fiechter, S.; Bogdanoff, P.; Tributsch, H.; Allee, R.; Lu, D.-. Catalysts for the Oxygen Reduction from Heat-Treated Iron (III) Tetramethoxyphenylporphyrin Chloride : Structure and Stability of Active Sites. *J. Phys. Chem. B* **2003**, *107*, 9034–9041.

(22) Shao, Y.; Dodelet, J.; Wu, G.; Zelenay, P. PGM-Free Cathode Catalysts for PEM Fuel Cells : A Mini-Review on Stability Challenges. *Adv. Mater*. **2019**, *31,* 1–8.

(23) Choi, C. H.; Baldizzone, C.; Grote, J.; Schuppert, A. K.; Jaouen, F.; Mayrhofer, K. J. J. Stability of Fe-N-C Catalysts in Acidic Medium Studied by Operando Spectroscopy. *Angew. Chem. Int. Ed. Engl.* **2015**, *54*, 12753–12757.

(24) Martinaiou, I.; Shahraei, A.; Grimm, F.; Zhang, H.; Wittich, C.; Klemenz, S.; Dolique, S. J.; Kleebe, H.; Stark, R. W.; Kramm, U. I. Effect of Metal Species on the Stability of Me-N-C Catalysts during Accelerated Stress Tests Mimicking the Start-up and Shut-down Conditions. *Electrochim. Acta* **2017**, *243*, 183–196.

(25) Goellner, V.; Baldizzone, C.; Schuppert, A.; Sougrati, M. T.; Mayrhofer, K.; Jaouen, F. Degradation of Fe / N / C Catalysts upon High Polarization in Acid Medium. *Phys. Chem. Chem. Phys.* **2014**, *16,* 18454–18462.

(26) Kreider, M. E.; Gallo, A.; Back, S.; Liu, Y.; Siahrostami, S.; Nordlund, D.; Sinclair, R.; Nørskov, J. K.; King, L. A.; Jaramillo, T. F. Precious Metal-Free Nickel Nitride Catalyst for the Oxygen Reduction Reaction. *ACS Appl. Mater. Interfaces* **2019**, *11*, 26863–26871.

(27) Wygant, B. R.; Kawashima, K.; Mullins, B. Catalyst or Precatalyst? The Effect of Oxidation on Transition Metal Carbide, Pnictide, and Chalcogenide Oxygen Evolution Catalysts. *ACS Energy Lett.* **2018**, *3*, 2956–2966.

(28) Avasarala, B.; Haldar, P. On the Stability of TiN-Based Electrocatalysts for Fuel Cell Applications. *Int. J. Hydrogen Energy* **2011**, *36*, 3965–3974.

(29) Chisaka, M.; Ando, Y.; Yamamoto, Y.; Itagaki, N. A Carbon-Support-Free Titanium Oxynitride Catalyst for Proton Exchange Membrane Fuel Cell Cathodes. *Electrochim. Acta* **2016**, *214*, 165–172.

(30) Cao, B.; Veith, G. M.; Diaz, R. E.; Liu, J.; Stach, E. A.; Adzic, R. R.; Khalifah, P. G. Cobalt Molybdenum Oxynitrides: Synthesis, Structural Characterization, and Catalytic Activity for the Oxygen Reduction Reaction. *Angewandte Chemie.* **2013**, *125*, 10953–10957.

(31) Cao, B.; Neuefeind, J. C.; Adzic, R. R.; Khalifah, P. G. Molybdenum Nitrides as Oxygen Reduction Reaction Catalysts: Structural and Electrochemical Studies. *Inorg. Chem*. **2015**, *54*, 2128–2136.

(32) Lee, K.-H.; Lee, Y.-W.; Kwak, D.-H.; Moon, J.-S.; Park, A.-R.; Hwang, E.-T.; Park, K.-W. Single-Crystalline Mesoporous Mo2N Nanobelts with an Enhanced Electrocatalytic Activity for Oxygen Reduction Reaction. *Mater. Lett.* **2014**, *124*, 231–234.

(33) Sun, T.; Wu, Q.; Che, R.; Bu, Y.; Jiang, Y.; Li, Y.; Yang, L.; Wang, X.; Hu, Z. Alloyed Co-Mo Nitride as High-Performance Electrocatalyst for Oxygen Reduction in Acidic Medium. *ACS Catal*. **2015**, *5*, 1857–1862.

(34) Zhong, H.; Zhang, H.; Liu, G.; Liang, Y.; Hu, J.; Yi, B. A Novel Non-Noble Electrocatalyst for PEM Fuel Cell Based on Molybdenum Nitride. *Electrochem. Commun*. **2006**, *8*, 707–712.

(35) Yuan, Y.; Amine, K.; Lu, J.; Shahbazian-yassar, R. Rechargeable Ion Batteries with in Situ Transmission Electron Microscopy. *Nat. Commun*. **2017**, *8*, 1–14.

(36) Ali-lo, H.; Louie, M. W.; Singh, M. R.; Li, L.; Casalongue, H. G. S.; Ogasawara, H.; Crumlin, E. J.; Liu, Z.; Bell, A. T.; Nilsson, A.; Friebel, D. Ambient-Pressure XPS Study of a Ni − Fe Electrocatalyst for the Oxygen Evolution Reaction. *J. Phys. Chem.C* **2016**, *120*, 2247-2253.

(37) Wyrzgol, S.A.; Schäfer, S.; Lee, S.; Lee, B.; Vece, M. D.; Li, X.; Seifert, S.; Winans, R.E.; Stutzmann, M.; Lercher, J. A; Vajda, S. Combined TPRx, in Situ GISAXS and GIXAS Studies of Model Semiconductor-Supported Platinum Catalysts in the Hydrogenation of Ethene. *Phys. Chem. Chem. Phys.* **2010**, *12*, 5585–5595.

(38) Janssen, J.; Rumpf, H.; Modrow, H.; Rablbauer, R.; Frommeyer, G.; Hormes, J. In Situ Study of the Surface Oxidation of FeCr Alloys Using Grazing Incidence X-Ray Absorption Spectroscopy (GIXAS) *Z. Anorg. Allg. Chem.* **2003**, *629*, 1701–1708.

(39) Farmand, M.; Landers, A. T.; Lin, J. C.; Feaster, J. T.; Beeman, J. W.; Ye, Y.; Clark, E. L.; Higgins, D.; Yano, J.; Davis, R. C.; Mehta, A.; Jaramillo, T. F.; Hahn, C.; Drisdell, W. S. Electrochemical Flow Cell Enabling Operando Probing of Electrocatalyst Surfaces By X-Ray Spectroscopy and Diffraction. *Phys. Chem. Chem. Phys.* **2019**, *21,* 5402-5408.

(40) Ravel, B.; Newville, M. ATHENA, ARTEMIS, HEPHAESTUS: Data Analysis for X-Ray Absorption Spectroscopy Using IFEFFIT. *J. Synchrotron Radiat.* **2005**, *12*, 537–541.

(41) Kresse, G.; Furthmüller, J. Efficient Iterative Schemes for Ab Initio Total-Energy Calculations Using a Plane-Wave Basis Set. *Phys. Chem. B* **1996**, *54*, 11169-11186.

(42) Blochl, P. E. Projector Augmented-Wave Method. *Phys. Rev. B* **1994**, *50*, 17953–17979.

(43) Sun, J.; Ruzsinszky, A.; Perdew, J. P. Strongly Constrained and Appropriately Normed Semilocal Density Functional. *PRL* **2015**, *036402*, 1–6.

(44) Jain, A.; Ong, S. P.; Hautier, G.; Chen, W.; Richards, W. D.; Dacek, S.; Cholia, S.; Gunter, D.; Skinner, D.; Ceder, G.; et al. Commentary : The Materials Project : A Materials Genome Approach to Accelerating Materials Innovation *APL mater.* **2013**, *1*, 1-11.

(45) Hammer, B.; Hansen, L. B.; Nørskov, J. K.; Improved Adsorption Energetics within Density-Functional Theory Using Revised Perdew-Burke-Ernzerhof Functionals. *Phys. Rev. B* **1999**, *59*, 7413–7421.

(46) Wang, L.; Maxisch, T.; Ceder, G. Oxidation Energies of Transition Metal Oxides within the GGA + U Framework. *Phys. Rev. B* **2006**, *73*, 1–6.

(47) Jain, A.; Hautier, G.; Ong, S. P.; Moore, C. J.; Fischer, C. C.; Persson, K. A.; Ceder, G. Formation Enthalpies by Mixing GGA and GGA + U Calculations. *Phys. Rev. B* **2011**, *84*, 1–10.

(48) Persson, K. A.; Waldwick, B.; Lazic, P.; Ceder, G. Prediction of Solid-Aqueous Equilibria : Scheme to Combine First-Principles Calculations of Solids with Experimental Aqueous States. *Phys. Rev. B* **2012**, *85*, 1–12.

(49) Rehr, J. J.; Kas, J. J.; Vila, F. D.; Prannge, M. P.; Jorissen, K. Parameter-Free Calculations of X-Ray Spectra with FEFF9. *Phys. Chem. Chem. Phys*. **2010**, *12*, 5503–5513.

(50) NIST Inorganic Crystal Structure Database, NIST Standard Reference Database Number 3, National Institute of Standards and Technology, Gaithersburg MD, 20899, https://doi.org/10.18434/M32147 (accessed Sept. 28, 2020).

(51) Liu, X.; Amiinu, I. S.; Liu, S.; Pu, Z.; Li, Wenqiang, Ye, B.; Tan, D.; Shichum, M. H_2O_2 - Assisted Synthesis of Porous N-Doped Graphene/Molybdenum Nitride Composites with Boosted Oxygen Reduction Reaction. *Adv. Mater. Interfaces* **2017**, *4*, 1-8.

(52) Saha, N. C.; Tompkins, H. G. Titanium Nitride Oxidation Chemistry: An x-Ray Photoelectron Spectroscopy Study. *J. App. Phys* **1992**, *7,* 3072-3079.

(53) Calvin, S. XAFS for Everyone; CRC Press: Boca Raton, FL, 2013.pp1 – 449.

(54) Kocha, S. S.; Zack, J. W.; Pivovar, B. S.; Richards, R. M.; Shinozaki, K. Oxygen Reduction Reaction Measurements on Platinum Electrocatalysts Utilizing Rotating Disk Electrode Technique. *J. Electrochem. Soc*. **2015**, *162*, F1144–F1158.

(55) Singh, A. K.; Zhou, L.; Shinde, A.; Suram, S. K.; Montoya, J. H.; Winston, D.; Gregoire, J. M.; Persson, K. A. Electrochemical Stability of Metastable Materials. *Chem Mat.* **2017**, *29,* 10159-10167.